

Dual-Reference Design for Holographic Coherent Diffraction Imaging*

David A. Barmherzig[†] Ju Sun[‡] Po-Nan Li[§] T.J. Lane[¶] Emmanuel J. Candès^{||}

June 27, 2019

Abstract

A new reference design is introduced for holographic coherent diffraction imaging. This consists in two references—“block” and “pinhole” shaped regions—placed adjacent to the imaging specimen. An efficient recovery algorithm is provided for the resulting holographic phase retrieval problem, which is based on solving a structured, overdetermined linear system. Analysis of the expected recovery error on noisy data, which is contaminated by Poisson shot noise, shows that this simple modification synergizes the individual references and hence leads to uniformly superior performance over single-reference schemes. Numerical experiments on simulated data confirm the theoretical prediction, and the proposed dual-reference scheme achieves a smaller recovery error than leading single-reference schemes.

1 Introduction

1.1 Holographic CDI and holographic phase retrieval

Coherent Diffraction Imaging (CDI) is a scientific imaging technique used for resolving nanoscale scientific specimens, such as macroviruses, proteins, and crystals [2]. In CDI, a coherent radiation source (often an X-ray beam) is incident on a specimen and gets diffracted. The resulting photon flux is then measured at a far-field detector, and the measured data are approximately proportional to the squared magnitudes of the Fourier transform of the wave field within the diffraction area. One can then determine the specimen’s structure by solving the *phase retrieval* problem, the mathematical inverse problem of recovering a signal from its squared Fourier magnitudes. The physical phase retrieval problem can be stated symbolically as

$$\begin{aligned} \text{Given} \quad & |\widehat{X}(\omega)|^2 \doteq \left| \int_{t \in T} X(t) e^{-i\langle \omega, t \rangle} \right|^2 \quad \text{for } \omega \in \Omega, \\ \text{Recover} \quad & X \end{aligned} \tag{1.1}$$

where T and Ω are the (possibly multidimensional) domains of the specimen and its Fourier transform, respectively. Since the detectors used in practical CDI have only a finite number of pixels, and algorithmic phase retrieval is often performed on digital computers, phase retrieval is frequently stated in the discrete form: in Eq. (1.1), Ω and T are finite-size arrays and the Fourier transform is implemented as the discrete Fourier transform. The discrete formulation is a reasonable proxy for the continuous formulation, as explained in Section A. We adopt this direct discrete formulation in this paper.

*A preliminary version is published in International Conference on Sampling and Applications, 2019 [1].

[†]Institute for Computational and Mathematical Engineering, Stanford University, Stanford, CA 94305, U.S.A.

[‡]Department of Mathematics, Stanford University, Stanford, CA 94305, U.S.A.

[§]Department of Electrical Engineering, Stanford University, Stanford, CA 94305, U.S.A.

[¶]SLAC National Accelerator Laboratory, Menlo Park, CA 94025, U.S.A.

^{||}Department of Mathematics and Department of Statistics, Stanford University, Stanford, CA 94305, U.S.A.

In a variant of CDI known as Holographic CDI, a “reference” portion of the diffraction area is a priori known from experimental design (e.g. see Figs. 1 and 2). Typically, the reference portion is simply a geometric shape cut out from the apparatus surrounding the specimen. The resulting inverse problem, in which a portion of the signal to be recovered is already known, is the *holographic phase retrieval* problem.

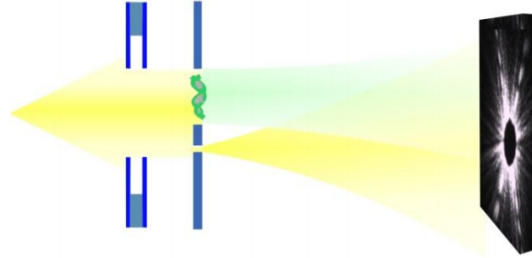


Figure 1: Holographic CDI schematic. The upper portion of the diffraction area contains the imaging specimen of interest, and the lower portion consists of a known “reference” shape. Image courtesy of [3].

For any reference choice satisfying mild assumptions, solving the holographic phase retrieval problem amounts to solving a structured linear system [4]. However, different reference choices will lead to different noise stability performances. Particularly, our previous work [4] revealed, both theoretically and empirically, the relative merits of two popular references: the block reference R_B (see Fig. 3a) performs favorably on data with low-frequency dominant spectra, whereas the pinhole reference (see Fig. 3b) has an edge for data with flat spectra. It is a natural question if the respectively advantages can be combined, and how.

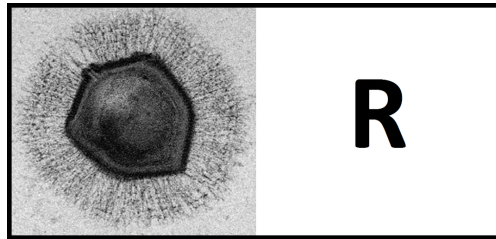


Figure 2: Schematic of the diffraction area in Holographic CDI containing a specimen and a known (single) reference portion. The specimen shown is the Mimivirus, courtesy of [5].

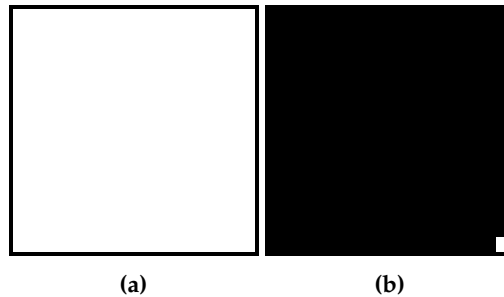


Figure 3: Two popular choices for the reference R shown in Fig. 2 are the block reference (Fig. 3a) and the pinhole reference (Fig. 3b).

1.2 Our contributions

In this paper, we answer the question in the affirmative and show that a simple augmentation of the block and pinhole references actually works as desired. A recovery algorithm is adapted from the referenced deconvolution algorithm introduced in [4]. Both theoretical (Section 3) and empirical (Section 4) results confirm the effectiveness of the proposed augmentation scheme. From hindsight, this is still a bit surprising, as the recovery error depends on the reference choice in a complicated manner; see Eq. (3.3).

1.3 A word on notation

We mostly use standard mathematical notations, with several special ones highlighted as below. Matlab notations $[A, B]$ and $[A; B]$ are used to mean horizontal and vertical concatenation of matrices, respectively. Similarly, notations such as $A(k, :)$ and $A(:, k)$ are used to index rows and columns of matrices, respectively. We use \otimes to denote the matrix Kronecker product.

2 Dual-reference design and recovery algorithm

2.1 Setup and algorithm

Definition 2.1. The block reference $R_B \in \mathbb{R}^{n \times n}$ and the pinhole reference $R_P \in \mathbb{R}^{n \times n}$ are defined respectively by

$$R_B(t_1, t_2) = 1, \quad t_1, t_2 \in \{0, \dots, n-1\}, \quad (2.1)$$

and

$$R_P(t_1, t_2) = \begin{cases} 1, & t_1 = t_2 = n-1 \\ 0, & \text{otherwise} \end{cases}. \quad (2.2)$$

The two references are visualized in Fig. 3a and Fig. 3b, respectively. Suppose that $X \in \mathbb{C}^{n \times n}$ is an “unknown” specimen. Consider $\mathcal{X} \in \mathbb{C}^{2n \times 2n}$ given by:

$$\mathcal{X} = \begin{bmatrix} X & R_B \\ R_P & \mathbf{0}_{n \times n} \end{bmatrix}, \quad (2.3)$$

where $\mathbf{0}_{n \times n}$ is the $n \times n$ all-zero matrix. We assume that the magnitudes of the entries of X are within the interval $[0, 1]$. By this convention, 0 values represent areas where the incoming beam is entirely blocked, and 1 values represent areas where the incoming beam passes through unimpeded—which would be “empty space”.

Suppose that $m \geq 4n - 1$ and that $Y = |\hat{\mathcal{X}}|^2 \in \mathbb{C}^{m \times m}$ are the magnitudes of the $m \times m$ oversampled Fourier transform of \mathcal{X} ¹. We seek to recover X from \tilde{Y} , which is a possibly noise-corrupted version of Y . We propose a recovery algorithm based on solving a structured linear system, which is effectively the *referenced deconvolution* algorithm introduced in [4] adapted to our current reference scheme.

1. Given \tilde{Y} , apply an inverse Fourier transform ($\mathbb{C}^{m \times m} \mapsto \mathbb{C}^{(4n-1) \times (4n-1)}$) to obtain $\tilde{A}_{\mathcal{X}}$, the noisy autocorrelation of \mathcal{X} .² This can be expressed as $\tilde{A}_{\mathcal{X}} = \frac{1}{m^2} F^* \tilde{Y} (F^*)^T$, where $F \in \mathbb{C}^{m \times (4n-1)}$ is given by $F(k, t) = e^{-2\pi i k t / m} \forall (k, t) \in \{0, \dots, m-1\} \times \{-(2n-1), \dots, 2n-1\}$.
2. Let $\mathcal{P}_1 = [\mathbf{0}_{n \times n}, I_n, \mathbf{0}_{n \times (2n-1)}]$ and $\mathcal{P}_2 = [I_n, \mathbf{0}_{n \times (3n-1)}]$. It follows that absent noise, $\mathcal{P}_1 \tilde{A}_{\mathcal{X}} \mathcal{P}_2^T \in \mathbb{R}^{n \times n}$ (resp., $\mathcal{P}_2 \tilde{A}_{\mathcal{X}} \mathcal{P}_1^T \in \mathbb{R}^{n \times n}$) is equal to the top-left quadrant of the cross-correlation of X and R_B (resp., X and R_P). We thus denote this as $\tilde{C}_{[X, R_B]}^{\circ}$ (resp., $\tilde{C}_{[X, R_P]}^{\circ}$).

¹Here, the absolute value notation on Y is understood in the pointwise sense. Also, we adopt the Matlab convention and assume the zero-frequency component is on the top-left corner of the data matrix.

²It is well-known that the inverse Fourier transform of the Fourier transform (with sufficient oversampling) magnitude squares of a signal is equal to the signal’s autocorrelation [6].

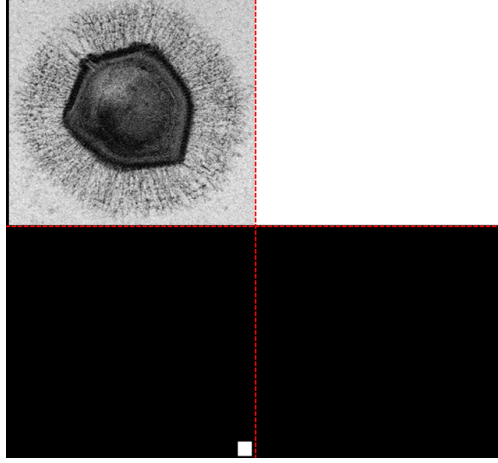


Figure 4: Schematic of the dual-reference. The red dotted line (added for illustration purposes) separates the four quadrants of the setup, as described by Eq. (2.3). The specimen shown is the mimivirus, courtesy of [5].

3. Let M_{R_B} (resp., M_{R_P}) $\in \mathbb{R}^{n^2 \times n^2}$ be the matrix satisfying $\text{vec}(C_{[X,R_B]}^\diamond) = M_{R_B} \text{vec}(X)$ (resp., $\text{vec}(C_{[X,R_P]}^\diamond) = M_{R_P} \text{vec}(X)$).³ It follows that $M_{R_B} = \mathbf{1}_L \otimes \mathbf{1}_L$, where $\mathbf{1}_L \in \mathbb{R}^{n \times n}$ is the lower-triangular matrix consisting of all ones on and below the main diagonal, and that $M_{R_P} = I_{n^2}$. Let $M = [M_{R_B}; M_{R_P}]$ and $b = [\text{vec}(\tilde{C}_{[X,R_B]}^\diamond); \text{vec}(\tilde{C}_{[X,R_P]}^\diamond)]$. The signal X is estimated as the solution to the least-squares problem

$$\tilde{X} = \arg \min_{X \in \mathbb{C}^{n \times n}} \|M \text{vec}(X) - b\|^2.$$

Analytically, this is given by

$$\text{vec}(\tilde{X}) = M^\dagger b = (M^T M)^{-1} M^T b.$$

Combining these steps and the well-known identity that $A = BCD \iff \text{vec}(A) = (D^T \otimes B) \text{vec}(C)$, we have

$$\text{vec}(\tilde{X}) = T_{R_B, P} \text{vec}(\tilde{Y}), \quad (2.4)$$

where

$$T_{R_B, P} = \frac{1}{m^2} M^\dagger \begin{bmatrix} \mathcal{P}_2 F^* \otimes \mathcal{P}_1 F^* \\ \mathcal{P}_1 F^* \otimes \mathcal{P}_2 F^* \end{bmatrix}. \quad (2.5)$$

Note that \tilde{X} is linear in \tilde{Y} and the proposed algorithm recovers X exactly when there is no noise.

2.2 Computation

Recall that $M \in \mathbb{R}^{2n^2 \times n^2}$. Thus, taking the inverse Fourier transform and solving the above linear system would cost $O(n^6 + m^2 \log m)$. Below, we show that for our specific $M = [\mathbf{1}_L \otimes \mathbf{1}_L; I_{n^2}]$, the cost can be significantly lower when the structure in M is exploited. We need the following result to proceed.

Lemma 2.2 (Chapter 1 of [7]). *Let $\mathbf{1}_L \in \mathbb{R}^{n \times n}$ be the lower triangular matrix with ones on and below the main diagonal. The singular value decomposition $\mathbf{1}_L = U \Sigma V^T$ is such that for any $s = 0, \dots, n-1$, U and V have columns given by*

$$U(t, s) = \frac{1}{\sqrt{\frac{n}{2} + \frac{1}{4}}} \sin \left\{ \frac{(s + \frac{1}{2})(t + 1)}{n + \frac{1}{2}} \pi \right\} \quad \text{for } t = 0, \dots, n-1$$

³The cross-correlations are linear in X , and hence such M_{R_B} and M_{R_P} exist for the noiseless cross-correlations $C_{[X,R_B]}^\diamond$ and $C_{[X,R_P]}^\diamond$.

$$V(t, s) = \frac{1}{\sqrt{\frac{n}{2} + \frac{1}{4}}} \cos \left\{ \frac{(s + \frac{1}{2})(t + \frac{1}{2})}{n + \frac{1}{2}} \pi \right\} \quad \text{for } t = 0, \dots, n-1$$

respectively, and Σ has diagonal entries given by

$$\sigma_s = \left[2 - 2 \cos \left(\frac{s + \frac{1}{2}}{n + \frac{1}{2}} \pi \right) \right]^{-1/2}.$$

Since $M = [\mathbf{1}_L \otimes \mathbf{1}_L; I_{n^2}]$ and writing the SVD of $\mathbf{1}_L$ as $\mathbf{1}_L = U\Sigma V^\top$ per [Lemma 2.2](#), we have

$$\begin{aligned} M^\dagger &= [(\mathbf{1}_L^\top \otimes \mathbf{1}_L^\top) (\mathbf{1}_L \otimes \mathbf{1}_L) + I_{n^2}]^{-1} [\mathbf{1}_L^\top \otimes \mathbf{1}_L^\top, I_{n^2}] \\ &= [(V\Sigma U^\top \otimes V\Sigma U^\top) (U\Sigma V^\top \otimes U\Sigma V^\top) + I_{n^2}]^{-1} [V\Sigma U^\top \otimes V\Sigma U^\top, I_{n^2}] \\ &= [(V\Sigma^2 V^\top) \otimes (V\Sigma^2 V^\top) + I_{n^2}]^{-1} [V\Sigma U^\top \otimes V\Sigma U^\top, I_{n^2}] \quad (\text{mixed product property}^4) \\ &= [(V \otimes V) (\Sigma^2 \otimes \Sigma^2) (V^\top \otimes V^\top) + I_{n^2}]^{-1} [(V \otimes V) (\Sigma \otimes \Sigma) (U^\top \otimes U^\top), I_{n^2}]. \end{aligned}$$

Now that $V \otimes V$ is an orthogonal matrix, it follows

$$[(V \otimes V) (\Sigma^2 \otimes \Sigma^2) (V^\top \otimes V^\top) + I_{n^2}]^{-1} = (V \otimes V) (\Sigma^2 \otimes \Sigma^2 + I_{n^2})^{-1} (V^\top \otimes V^\top).$$

Thus,

$$M^\dagger = \left[(V \otimes V) (\Sigma^2 \otimes \Sigma^2 + I_{n^2})^{-1} (\Sigma \otimes \Sigma) (U^\top \otimes U^\top), (V \otimes V) (\Sigma^2 \otimes \Sigma^2 + I_{n^2})^{-1} (V^\top \otimes V^\top) \right]. \quad (2.6)$$

By [Eq. \(2.5\)](#),

$$\begin{aligned} T_{R_B, P} &= \frac{1}{m^2} (V \otimes V) \left[(\Sigma^2 \otimes \Sigma^2 + I_{n^2})^{-1} (\Sigma \otimes \Sigma) (U^\top \otimes U^\top) (\mathcal{P}_2 F^* \otimes \mathcal{P}_1 F^*) \right. \\ &\quad \left. + (\Sigma^2 \otimes \Sigma^2 + I_{n^2})^{-1} (V^\top \otimes V^\top) (\mathcal{P}_1 F^* \otimes \mathcal{P}_2 F^*) \right] \\ &= \frac{1}{m^2} (V \otimes V) \left[(\Sigma^2 \otimes \Sigma^2 + I_{n^2})^{-1} (\Sigma \otimes \Sigma) (U^\top \mathcal{P}_2 F^* \otimes U^\top \mathcal{P}_1 F^*) \right. \\ &\quad \left. + (\Sigma^2 \otimes \Sigma^2 + I_{n^2})^{-1} (V^\top \mathcal{P}_1 F^* \otimes V^\top \mathcal{P}_2 F^*) \right]. \end{aligned} \quad (2.7)$$

For the final computation, we make repeated use of the property $A = BCD \iff \text{vec}(A) = (D^\top \otimes B) \text{vec}(C)$ to obtain that

$$\begin{aligned} \text{vec}(\tilde{X}) &= T_{R_B, P} \text{vec}(\tilde{Y}) \\ &= \frac{1}{m^2} (V \otimes V) \underbrace{(\Sigma^2 \otimes \Sigma^2 + I_{n^2})^{-1} \left[\text{vec}(\Sigma U^\top \mathcal{P}_1 F^* \tilde{Y} \bar{F} \mathcal{P}_2^\top U \Sigma) + \text{vec}(V^\top \mathcal{P}_2 F^* \tilde{Y} \bar{F} \mathcal{P}_1^\top V) \right]}_{\doteq \text{vec}(Q) \text{ for a } Q \in \mathbb{R}^{n^2 \times n^2}} \\ &= \frac{1}{m^2} \text{vec}(V Q V^\top), \end{aligned}$$

which obviously can be computed in $O(n^3 + m^2 \log m)$ time, as against $O(n^6 + m^2 \log m)$.

3 Analysis of the recovery error

For any data \tilde{Y} following a known probability distribution, it follows from [Eq. \(2.4\)](#) that

$$\mathbb{E} \|\tilde{X} - X\|_F^2 = \left\langle T_R^* T_R, \mathbb{E} \left[\text{vec}(\tilde{Y}) - \text{vec}(Y) \right] \left[\text{vec}(\tilde{Y}) - \text{vec}(Y) \right]^* \right\rangle, \quad (3.1)$$

⁴For any A, B and C, D of compatible dimensions, $(A \otimes B)(C \otimes D) = (AC) \otimes (BD)$.

where $\|\cdot\|_F^2$ denotes the Frobenius norm, and $\langle \cdot, \cdot \rangle$ denotes the Frobenius inner product.

In CDI, measurements of photon flux at the detector are subject to quantum shot noise. This is due to intrinsic quantum fluctuations which cannot be removed in any measurement system. The resulting measurements follow the Poisson shot noise distribution given by

$$\tilde{Y} \sim_{\text{ind}} \frac{\|Y\|_1}{N_p} \text{Pois}\left(\frac{N_p}{\|Y\|_1} Y\right), \quad (3.2)$$

where N_p is the expected (or nominal) number of photons reaching the detector, and $\|Y\|_1$ is understood as the ℓ_1 norm of a vectorized version of Y [8]. As derived in [4], under this model

$$\mathbb{E}\|\tilde{X} - X\|_F^2 = \frac{\|Y\|_1}{N_p} \langle S_{R_B, P}, Y \rangle, \quad (3.3)$$

where

$$S_{R_B, P} = \text{reshape}(\text{diag}(T_R^* T_R), m, m), \quad (3.4)$$

and $\text{reshape}(\cdot, m, m)$ is the columnwise vector-to-matrix reshaping operator.

In the recovery error Eq. (3.3), both Y and $S_{R_B, P}$ depend on the references in use. Empirically, for low-frequency dominant X (e.g., CDI specimens shown in Fig. 2 and Fig. 7), the spectrum of Y is similar to that of X , up to small variations in the magnitudes; see Fig. 5. This stability property of spectrum can be

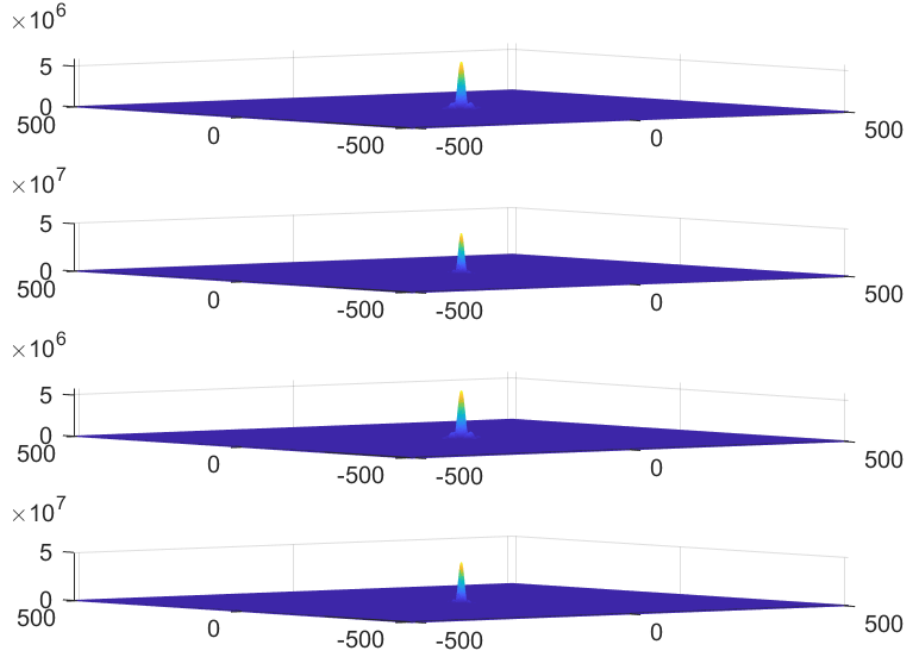


Figure 5: Top to bottom: squared magnitudes of the Fourier transform of the mimivirus [5] itself, and that when the mimivirus is augmented with the block, pinhole, and dual-references, respectively (with $n = 64$, and $m = 1024$). These four spectra exhibit similar low-frequency dominance, and have entries of similar orders of magnitude.

formally established for the single-reference setup $[X, R]$ (by expanding $|\widehat{[X, R]}|^2$ [4]), and likewise for our dual-reference setup. In contrast, the weighting factors in S_R can vary by several orders of magnitude for

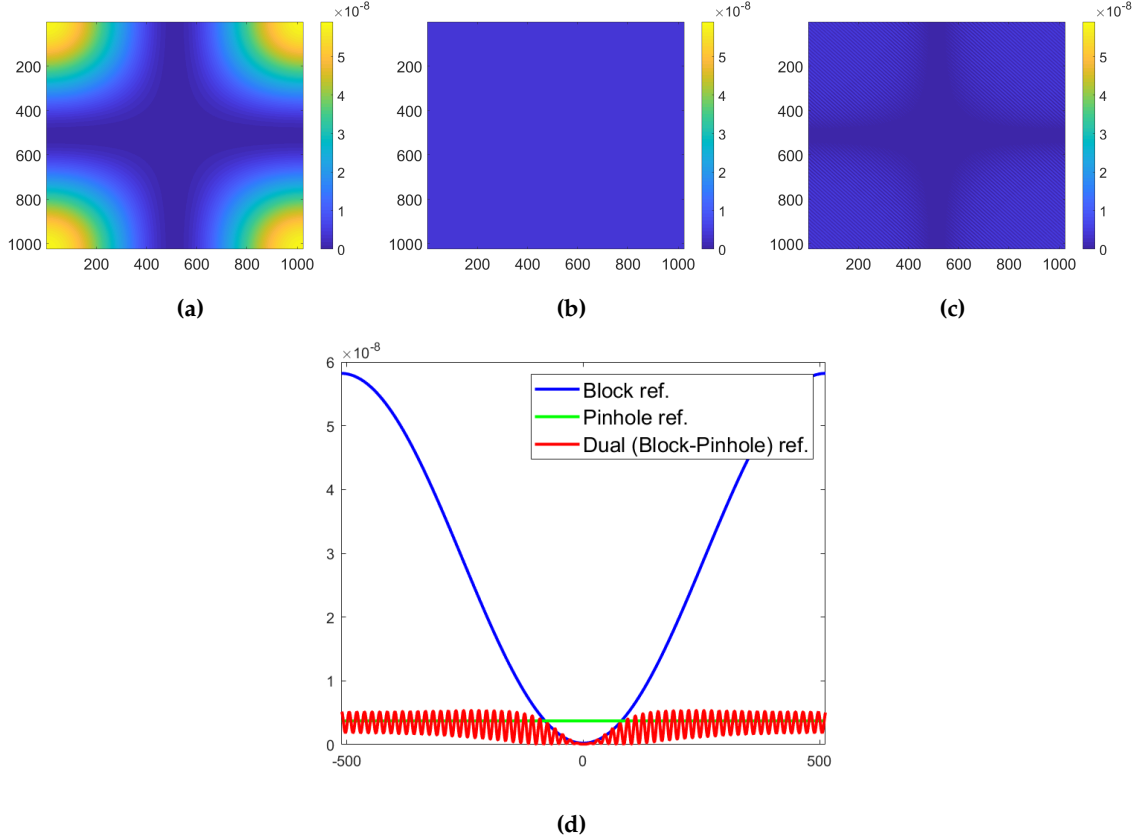


Figure 6: The top row shows colormap plots of the weighting factors S_R for the block, pinhole, and dual references, respectively, when $n = 64$ and $m = 1024$. The bottom plot shows the three weighting factors along the (four identical) bordering cross-sections of the colormap plots.

different reference schemes, as shown in Fig. 6. Hence, the influence of the reference scheme on the recovery error is largely determined by S_R .

We now derive an convenient analytical expression for $S_{R_{B,P}}$.

Proposition 3.1. For any $k_1, k_2 \in \{0, \dots, m-1\}$, $S_{R_{B,P}}(k_1, k_2)$ is equal to

$$\frac{1}{m^4} \sum_{r,s=0}^{n-1} \left| \frac{\sigma_r \sigma_s}{\sigma_r^2 \sigma_s^2 + 1} u_r^\top (\mathcal{P}_2 F^*)(:, k_1) u_s^\top (\mathcal{P}_1 F^*)(:, k_2) + \frac{1}{\sigma_r^2 \sigma_s^2 + 1} v_r^\top (\mathcal{P}_1 F^*)(:, k_1) v_s^\top (\mathcal{P}_2 F^*)(:, k_2) \right|^2. \quad (3.5)$$

Proof. From Eq. (3.4), $S_{R_{B,P}}(k_1, k_2) = \|T'_R(:, mk_1 + k_2)\|^2$ and thus we are interested in the squared column norms of T_R . Since $V \otimes V$ is an orthogonal matrix and the Euclidean norm is orthogonally invariant, by Eq. (2.7), it is sufficient to consider the squared column norms of

$$T'_R = \frac{1}{m^2} \left[(\Sigma^2 \otimes \Sigma^2 + I_{n^2})^{-1} (\Sigma \otimes \Sigma) (U^\top \mathcal{P}_2 F^* \otimes U^\top \mathcal{P}_1 F^*) + (\Sigma^2 \otimes \Sigma^2 + I_{n^2})^{-1} (V^\top \mathcal{P}_1 F^* \otimes V^\top \mathcal{P}_2 F^*) \right].$$

For any $(k_1, k_2) \in \{0, 1, \dots, m-1\} \times \{0, 1, \dots, m-1\}$ and the corresponding $k = mk_1 + k_2$,

$$\begin{aligned} & \|T'_R(:, k)\|^2 \\ &= \frac{1}{m^4} \sum_{r,s=0}^{n-1} \left| \frac{\sigma_r \sigma_s}{\sigma_r^2 \sigma_s^2 + 1} [U^\top \mathcal{P}_2 F^*](r, k_1) [U^\top \mathcal{P}_1 F^*](s, k_2) + \frac{1}{\sigma_r^2 \sigma_s^2 + 1} [V^\top \mathcal{P}_1 F^*](r, k_1) [V^\top \mathcal{P}_2 F^*](s, k_2) \right|^2 \end{aligned}$$

$$= \frac{1}{m^4} \sum_{r,s=0}^{n-1} \left| \frac{\sigma_r \sigma_s}{\sigma_r^2 \sigma_s^2 + 1} u_r^\top (\mathcal{P}_2 F^*)(:, k_1) u_s^\top (\mathcal{P}_1 F^*)(:, k_2) + \frac{1}{\sigma_r^2 \sigma_s^2 + 1} v_r^\top (\mathcal{P}_1 F^*)(:, k_1) v_s^\top (\mathcal{P}_2 F^*)(:, k_2) \right|^2,$$

as claimed. \blacksquare

In Fig. 6, we compare the S_R 's for the single-reference setup (either the pinhole or the block reference), with that of our dual-reference setup. For the single-reference setup $[X, R]$, [4] showed that among three reference choices, the block and pinhole references perform best for low-frequency dominant Y and flat-spectrum Y , respectively. Surprisingly, the simple idea of including the two references simultaneously and solving the resulting stacked linear system helps to combine the strengths. Indeed, as shown in Fig. 6, $S_{R_B, P}$ approximates the minimum of S_{R_B} and S_{R_P} uniformly over the entire frequency spectrum.

4 Numerical simulations

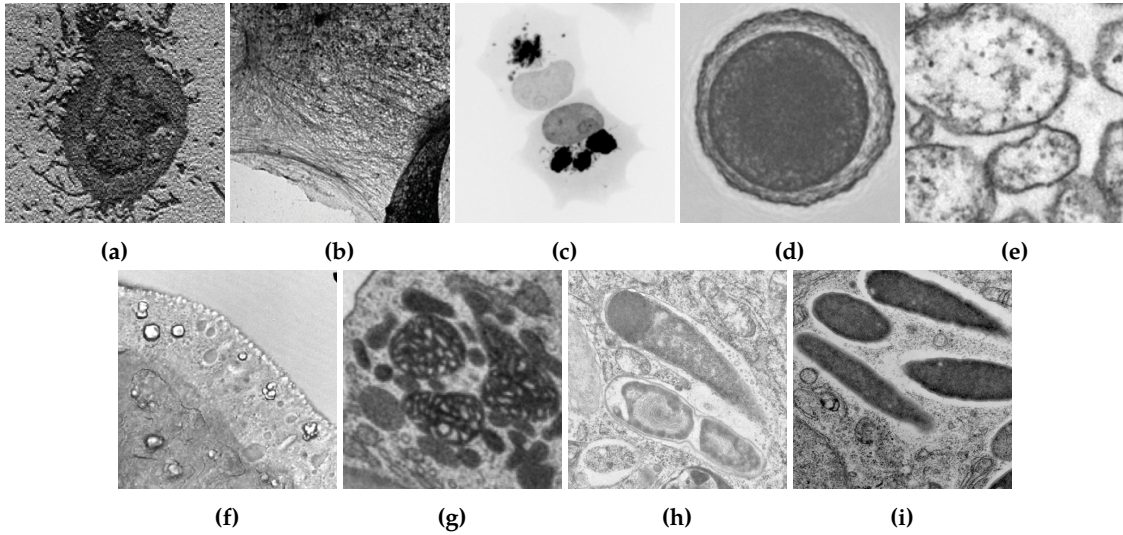


Figure 7: CDI specimen images used for numerical simulations in Table 1. Shown are specimens of influenza virus [9], stroma cells [9], mCherry proteins [10], 2-cell embryo [11], oocytes [11], *S. pistillata* [12], in-cellular aragonite crystal [13], salmonella WT [14], and sifA salmonella strain [14], respectively.

For numerical evaluation of the proposed dual-reference scheme, we use images of 9 different specimens from diverse sources: influenza virus [9], stroma cells [9], mCherry proteins [10], 2-cell embryo [11], oocytes [11], *S. pistillata* [12], in-cellular aragonite crystal [13], salmonella WT [14], and sifA salmonella strain [14].

To set up, each image is resized to 64×64 , and the pixel values are normalized to $[0, 1]$. The oversampled Fourier transform is taken to be of size 1024×1024 , and the collected noisy data \hat{Y} obeys the Poisson shot noise model defined in Eq. (3.2). The nominal number of photons is set as $N_p = 1000 \times 1024^2$.

We compare the proposed dual-reference design with the single-reference design studied in [4]. Specifically, we consider the configuration $[X, R]$ with R being either the pinhole or the block reference. The images are retrieved by the referenced deconvolution algorithm. We also report the performance of the classic hybrid input output (HIO) algorithm on these images, with or without an augmented reference. Performance is measured by the relative recovery error, defined as

$$\varepsilon \doteq \frac{\|X - \hat{X}\|^2}{\|X\|^2}. \quad (4.1)$$

The detailed recovery errors for the various schemes are tabulated in Table 1. It is evident that the dual-reference scheme performs consistently better than other schemes.

Table 1: Empirical and expected values (shown in brackets) for the relative squared errors $\|\tilde{X} - X\|_F^2 / \|X\|_F^2$ using various recovery methods. The methods are referenced deconvolution with a block, pinhole, and dual-reference, as well as HIO with no reference (HIO(a)), with a block reference (HIO(b)), and with a pinhole reference (HIO(c)). The error values are the reported values rescaled by 10^{-4} . Test images X of size 64×64 pixels are the mimivirus shown in Fig. 2, and the images shown in Fig. 7. Simulated photon flux data is of size 1024×1024 , with $N_p = 1000(1024^2)$ (i.e. 1000 photons per pixel).

Image	Block Ref.	Pinhole Ref.	Dual Ref.	HIO (a)	HIO (b)	HIO (c)
Mimivirus	3.70 (3.79)	46.9 (63.8)	1.51 (1.45)	93.7	42.8	168.1
Influenza	18.7 (18.5)	50.7 (31.4)	4.64 (4.70)	695.7	219.6	401.1
Stroma cells	9.19 (8.91)	23.1 (44.1)	2.78 (2.63)	1607.0	110.8	2204.8
mCherry proteins	1.84 (1.84)	139.5 (131.5)	0.927 (0.908)	403.1	19.1	162.4
Embryo	6.30 (6.29)	54.2 (53.8)	2.62 (2.71)	642.4	140.9	672.5
Oocytes	7.01 (6.84)	44.1 (78.3)	2.66 (2.70)	883.1	96.9	895.5
S. pistallata	4.02 (3.93)	148.8 (83.7)	1.29 (1.31)	335.6	51.2	87.4
Aragonite	11.6 (11.5)	52.1 (34.6)	4.41 (4.41)	1767.3	181.7	971.1
Salmonella WT	9.07 (8.81)	44.3 (60.1)	3.33 (2.97)	708.0	189.8	389.0
sifA	7.27 (7.15)	42.6 (54.6)	2.82 (2.86)	1765.6	221.2	678.7

5 Conclusions

We have proposed a novel dual-reference scheme for holographic CDI, together with a recovery algorithm which provides exact recovery in the noiseless setting. For data corrupted by Poisson shot noise, the dual-reference combines the best features of the block and pinhole references. Numerical experiments on simulated CDI data show the dual-reference scheme provides a smaller recovery error than the leading (single) reference schemes.

Acknowledgments

The authors are very grateful to Walter Murray, Gordon Wetzstein for many guiding discussions throughout this research.

Appendices

A Connection between the continuous and discrete settings

The computational imaging literature often only describe the continuous formulation of CDI imaging, without touching on the intrinsic discretization issue due to the finite-grid photon detector and computational feasibility. For the sake of completeness, here we clarify the relevant issues. An exposition similar to Section A.1 can also be found in Sec. 5.6 of [15].

A.1 Sampling at the detector

In CDI setup, suppose the detector is sufficiently far away from the specimen of interest so that the well known *Fraunhofer approximation* applies. Denote the (electromagnetic) field transmitted through the specimen as $I(x, y) \doteq f(x, y, 0)$. Then, the field intensity at the far-field (i.e., $z \gg 0$) detector can be approximated as

$$|f(x, y, z)|^2 \approx \frac{1}{\lambda^2 z^2} |\hat{I}\left(\frac{x}{\lambda z}, \frac{y}{\lambda z}\right)|^2,$$

where λ is the wavelength of the electromagnetic radiation and \widehat{I} is the continuous 2D Fourier transform of I :

$$\widehat{I}(u, v) = \int_{\mathbb{R}^2} I(x, y) e^{-i2\pi(ux+vy)} dx dy.$$

The detector consists of an array of $\Delta \times \Delta$ square pixel areas, each of which counts the incident photons. Let p, q index the 2D array of pixels. The radiation energy received at the (p, q) -th pixel area ($p, q \in \mathbb{Z}$) is given by

$$\frac{\tau\mu}{\lambda^2 z^2} \int_{(x,y) \in [-\Delta/2, \Delta/2]^2} \left| \widehat{I} \left(\frac{p\Delta + x}{\lambda z}, \frac{q\Delta + y}{\lambda z} \right) \right|^2 dx dy,$$

where τ is the collection duration and μ is the detector quantum efficiency. When Δ is sufficiently small, the above integral can be well approximated by

$$\frac{\Delta^2 \tau \mu}{\lambda^2 z^2} \left| \widehat{I} \left(\frac{p\Delta}{\lambda z}, \frac{q\Delta}{\lambda z} \right) \right|^2, \quad (\text{A.1})$$

which can be treated as the mean number of photons measured by the (p, q) pixel location in the collection duration τ .

A.2 Continuous to discrete Fourier analysis

So measurements of CDI are effectively samples of the spectrum $|\widehat{I}|^2$ at discrete locations $(p\Delta', q\Delta')$ for $p, q \in \mathbb{Z}$, where $\Delta' \doteq \Delta / (\lambda z)$. We will write these samples collectively as Y where $Y[p, q] = |\widehat{I}(p\Delta', q\Delta')|^2$. In practice, phase retrieval is the problem of recovering the complex phases of Y , from Y and additional knowledge about I .

Recovering these spectrum samples is crucial, as they can be used for recovering I itself. In practical CDI, I is always compactly supported. Without loss of generality, we assume the support is $[-B/2, B/2] \times [-B/2, B/2]$. Since \widehat{I} and I are related by 2D continuous Fourier transform, 2D sampling theorem (see, e.g., Chapter 2 of [16]) implies that whenever

$$\frac{\Delta}{\lambda z} \leq \frac{1}{B} \iff \Delta \leq \frac{\lambda z}{B}, \quad (\text{A.2})$$

I can be recovered from samples $\widehat{I}(p\Delta', q\Delta')$ for all $p, q \in \mathbb{Z}$ via interpolation.

Performing continuous-time Fourier transform on $\widehat{I}(u, v) \sum_{p,q \in \mathbb{Z}} \delta(u - p\Delta', v - q\Delta')$ reduces to performing discrete-time Fourier transform (DTFT) on $\widehat{I}[p, q]$, where δ denotes the delta function, either 1D or 2D depending on the context. Moreover, the samples of DTFT($\widehat{I}[p, q]$), i.e., samples of I , can be computed via discrete Fourier transform. This serves as a high-level justification of our discrete formulation, and is also well established in the digital signal processing literature.

Now we work out the quantitative details. The continuous-time (inverse) Fourier transform on the sampled $\widehat{I}(u, v) \sum_{p,q \in \mathbb{Z}} \delta(u - p\Delta', v - q\Delta')$ is

$$\begin{aligned} J(x, y) &= \int_{\mathbb{R}^2} \widehat{I}(u, v) \sum_{p,q \in \mathbb{Z}} \delta(u - p\Delta', v - q\Delta') e^{i2\pi(ux+vy)} dudv \\ &= \int_{\mathbb{R}^2} \sum_{p,q \in \mathbb{Z}} \widehat{I}(p\Delta', q\Delta') \delta(u - p\Delta', v - q\Delta') e^{i2\pi(ux+vy)} dudv \\ &= \sum_{p,q \in \mathbb{Z}} \widehat{I}(p\Delta', q\Delta') \int_{\mathbb{R}^2} \delta(u - p\Delta', v - q\Delta') e^{i2\pi(ux+vy)} dudv \\ &= \sum_{p,q \in \mathbb{Z}} \widehat{I}(p\Delta', q\Delta') e^{i2\pi(p\Delta'x + q\Delta'y)}, \end{aligned}$$

where at the last step we used the sifting property of the δ function. We recognize that the last equation represents the (exponential-conjugate) 2D discrete-time Fourier transform on the discrete sequence $\widehat{I}[p, q]$, with the frequency axes rescaled by a factor $2\pi\Delta'$.

Practical detectors have only finite sizes. So we do not have access to the 2D discrete sequence $\widehat{I}[p, q]$, but a truncated version $\widehat{I}_T[p, q]$ so that:

$$\widehat{I}_T[p, q] = \begin{cases} \widehat{I}[p, q] & |p| \leq D \text{ and } |q| \leq D \\ 0 & \text{otherwise} \end{cases},$$

where we assume the detector consists of $(2D + 1) \times (2D + 1)$ pixels. Thus, at best we can compute an approximation \widetilde{J} to J :

$$\widetilde{J}(x, y) = \sum_{p, q \in \mathbb{Z}: |p| \leq D, |q| \leq D} \widehat{I}(p\Delta', q\Delta') e^{i2\pi(p\Delta'x + q\Delta'y)}. \quad (\text{A.3})$$

When the spectrum \widehat{I} decays sufficiently fast—which is often true in practice—and $2D + 1$ (size of the detector) is relatively large, $\|J - \widetilde{J}\|_{L_1}$ tends to be small. Taking the discrete Fourier transform on $\widehat{I}_T[p, q]$ (for convenience, we take a less standard convention)

$$\sum_{p=-D}^D \sum_{q=-D}^D \widehat{I}_T[p, q] e^{i2\pi(pn_1 + qn_2)/(2D+1)} \quad (\text{A.4})$$

obviously computes \widetilde{J} at locations $\left(\frac{n_1}{(2D+1)\Delta'}, \frac{n_2}{(2D+1)\Delta'}\right)$ for all $n_1, n_2 \in \mathbb{Z}$ with $|n_1| \leq D, |n_2| \leq D$.

To sum up, when the sampling interval on the detector is sufficiently small ($\Delta \leq \lambda z/B$) and the detector contains sufficiently large number of pixels (i.e., D large), the discrete formulation for CDI is a reasonable proxy to the continuous formulation. Particularly, recovering the phases of the frequency samples helps to approximate the original field I at discrete sampled points.

A.3 Continuous vs. discrete signal recovery

In this subsection, we sketch the correspondence between the discrete signal recovered via the recovery algorithm of this paper versus the continuous specimen signal. Firstly, we show that the discrete autocorrelation obtained is (approximately) a sampled version of the continuous autocorrelation. Secondly, we discuss how the discrete signal X recovered from the discrete autocorrelation approximates the continuous specimen signal I .

Let A_I denote the autocorrelation of I , i.e.,

$$A_I(s, t) = \int_{\mathbb{R}^2} I(x, y) \overline{I(x-s, y-t)} dx dy.$$

Thanks to the convolution theorem of Fourier transform,

$$|\widehat{I}(u, v)|^2 = \int_{\mathbb{R}^2} A_I(x, y) e^{-i2\pi(ux+vy)} dx dy,$$

i.e., squared Fourier magnitudes of I are the Fourier transform of A_I .

As discussed above, sampling occurs at the detector. On one hand, due to the convolution theorem of Fourier transform,

$$\int_{\mathbb{R}^2} |\widehat{I}(u, v)|^2 \sum_{p, q \in \mathbb{Z}} \delta(u - p\Delta', v - q\Delta') e^{i2\pi(ux+vy)} dudv$$

$$\begin{aligned}
&= \int_{\mathbb{R}^2} |\widehat{I}(u, v)|^2 e^{i2\pi(ux+vy)} dudv * \\
&\quad \int_{\mathbb{R}^2} \sum_{p, q \in \mathbb{Z}} \delta(u - p\Delta', v - q\Delta') e^{i2\pi(ux+vy)} dudv \\
&= A_I(x, y) * \frac{1}{\Delta'^2} \sum_{k, \ell \in \mathbb{Z}} \delta\left(x - \frac{k}{\Delta'}, y - \frac{\ell}{\Delta'}\right).
\end{aligned}$$

On the other hand, similar to the argument in [Section A.2](#),

$$\int_{\mathbb{R}^2} |\widehat{I}(u, v)|^2 \sum_{p, q \in \mathbb{Z}} \delta(u - p\Delta', v - q\Delta') e^{i2\pi(ux+vy)} dudv = \sum_{p, q \in \mathbb{Z}} \left| \widehat{I}(p\Delta', q\Delta') \right|^2 e^{i2\pi(p\Delta'x + q\Delta'y)}.$$

Thus,

$$A_I(x, y) * \frac{1}{\Delta'^2} \sum_{k, \ell \in \mathbb{Z}} \delta\left(x - \frac{k}{\Delta'}, y - \frac{\ell}{\Delta'}\right) = \sum_{p, q \in \mathbb{Z}} \left| \widehat{I}(p\Delta', q\Delta') \right|^2 e^{i2\pi(p\Delta'x + q\Delta'y)}. \quad (\text{A.5})$$

For sanity check, both sides are spatially periodic with period $(1/\Delta', 1/\Delta')$. Now since I is supported on $[-B/2, B/2] \times [-B/2, B/2]$, A_I is supported on $[-B, B] \times [-B, B]$. So whenever

$$\frac{1}{\Delta'} \geq 2B \iff \frac{\Delta}{\lambda z} \leq \frac{1}{2B}, \quad (\text{A.6})$$

there is no aliasing and we can focus on the region $[-B, B] \times [-B, B]$ which contains a scaled version of A_I .

To account for the truncation effect, we again assume $|\widehat{I}(p\Delta', q\Delta')|^2$ gets truncated whenever $|p| > D$ or $|q| > D$ for a certain $D \in \mathbb{N}$. Then, taking the discrete Fourier transform on the truncated sequence, i.e.,

$$\sum_{p=-D}^D \sum_{q=-D}^D \left| \widehat{I}(p\Delta', q\Delta') \right|^2 e^{i2\pi(pn_1 + qn_2)/(2D+1)} \quad (\text{A.7})$$

approximates the values of A_I at locations $\left(\frac{n_1}{(2D+1)\Delta'}, \frac{n_2}{(2D+1)\Delta'}\right)$ for all $n_1, n_2 \in \mathbb{Z}$ with $|n_1| \leq D$ and $|n_2| \leq D$.

Having obtained an (approximate) sampled version of the continuous autocorrelation, the relationship between the corresponding discrete signal X and the continuous specimen signal exactly corresponds to the midpoint rule approximation of an integral (e.g. see [17]). Specifically, it was shown in [4] that the relationship between X and $A_{[X, R]}$ that governs signal recovery is given by:

$$A_{[X, R]}(s_1, -n + s_2) = \sum_{t_1=0}^{n-1} \sum_{t_2=0}^{n-1} X(t_1, t_2) \overline{R(t_1 - s_1, t_2 - s_2)}, \quad (\text{A.8})$$

for $s_1, s_2 \in \{-(n-1), \dots, 0\}$ (see Eq. 2.10 of [4] for this exact setup). Now consider the continuous counterpart (with analogous notational conventions), i.e. a continuous specimen and reference composite given by $[X, R] \in [0, B] \times [0, 2B]$. The continuous partial autocorrelation can analogously be derived using the procedure in [4], and is given by:

$$A_{[X, R]}(s_1, -B + s_2) = \int_{t_1=0}^B \int_{t_2=0}^B X(t_1, t_2) \overline{R(t_1 - s_1, t_2 - s_2)}, \quad (\text{A.9})$$

for $s_1, s_2 \in [-B, 0]$. The points of the discrete X in [Eq. \(A.8\)](#) serve to approximate the continuous expression in [Eq. \(A.9\)](#) via the midpoint rule approximation for integration (up to a scaling factor). Thus, in the limit that the number of points on X in the summation [Eq. \(A.8\)](#) approaches a continuum, the discrete and continuous counterparts of X exactly coincide.

References

- [1] D. A. Barmherzig, J. Sun, E. J. Candès, T. J. Lane, and P.-N. Li, "Dual-reference design for holographic phase retrieval," in *International Conference on Sampling and Applications*, 2019.
- [2] J. Miao, P. Charalambous, J. Kirz, and D. Sayre, "Extending the methodology of X-ray crystallography to allow imaging of micrometre-sized non-crystalline specimens," *Nature*, vol. 400, pp. 342–344, jul 1999.
- [3] M. Saliba, T. Latychevskaia, J. Longchamp, and H. Fink, "Fourier Transform Holography: A Lensless Non-Destructive Imaging Technique," *Microscopy and Microanalysis*, vol. 18, no. S2, pp. 564–565, 2012.
- [4] D. A. Barmherzig, J. Sun, E. J. Candès, T. J. Lane, and P.-N. Li, "Holographic Phase Retrieval and Optimal Reference Design," *arXiv e-prints*, p. arXiv:1901.06453, Jan. 2019.
- [5] E. Ghigo, J. Kartenbeck, P. Lien, L. Pelkmans, C. Capo, J.-L. Mege, and D. Raoult, "Ameobal Pathogen Mimivirus Infects Macrophages through Phagocytosis," *PLOS Pathogens*, vol. 4, no. 6, pp. 1–17, 2008. [Online]. Available: <https://doi.org/10.1371/journal.ppat.1000087>
- [6] A. V. Oppenheim and R. W. Schaffer, *Discrete-Time Signal Processing*, 3rd ed. Upper Saddle River, NJ, USA: Prentice Hall Press, 2009.
- [7] G. Strang, *Computational Science and Engineering*. Wellesley, MA, USA: Wellesley-Cambridge Press, 2012.
- [8] I. S. Wahyutama, G. K. Tadesse, A. Tünnermann, J. Limpert, and J. Rothhardt, "Influence of detector noise in holographic imaging with limited photon flux," *Opt. Express*, vol. 24, no. 19, pp. 22 013–22 027, sep 2016. [Online]. Available: <http://www.opticsexpress.org/abstract.cfm?URI=oe-24-19-22013>
- [9] D. Kim, T. J. Deerinck, Y. M. Sigal, H. P. Babcock, M. H. Ellisman, and X. Zhuang, "Correlative stochastic optical reconstruction microscopy and electron microscopy," *PLOS ONE*, vol. 10, no. 4, pp. 1–20, 04 2015. [Online]. Available: <https://doi.org/10.1371/journal.pone.0124581>
- [10] P. Paszkowski, R. S. Noyce, and D. H. Evans, "Live-cell imaging of vaccinia virus recombination," *PLOS Pathogens*, vol. 12, no. 8, pp. 1–28, 08 2016. [Online]. Available: <https://doi.org/10.1371/journal.ppat.1005824>
- [11] M. Eitel, L. Guidi, H. Hadrys, M. Balsamo, and B. Schierwater, "New insights into placozoan sexual reproduction and development," *PLOS ONE*, vol. 6, no. 5, pp. 1–9, 05 2011. [Online]. Available: <https://doi.org/10.1371/journal.pone.0019639>
- [12] A. Venn, E. Tambutte, M. Holcomb, D. Allemand, and S. Tambutte, "Live tissue imaging shows reef corals elevate ph under their calcifying tissue relative to seawater," *PLOS ONE*, vol. 6, no. 5, pp. 1–9, 05 2011. [Online]. Available: <https://doi.org/10.1371/journal.pone.0020013>
- [13] T. D. Mayorova, C. L. Smith, K. Hammar, C. A. Winters, N. B. Pivovarova, M. A. Aronova, R. D. Leapman, and T. S. Reese, "Cells containing aragonite crystals mediate responses to gravity in trichoplax adhaerens (placozoa), an animal lacking neurons and synapses," *PLOS ONE*, vol. 13, no. 1, pp. 1–20, 01 2018. [Online]. Available: <https://doi.org/10.1371/journal.pone.0190905>
- [14] R. Rajashekar, D. Liebl, D. Chikkaballi, V. Liss, and M. Hensel, "Live cell imaging reveals novel functions of salmonella enterica spi2-t3ss effector proteins in remodeling of the host cell endosomal system," *PLOS ONE*, vol. 9, no. 12, pp. 1–29, 12 2014. [Online]. Available: <https://doi.org/10.1371/journal.pone.0115423>
- [15] M. Guizar Sicairos, "Methods for coherent lensless imaging and x-ray wavefront measurements," Ph.D. dissertation, University of Rochester. Institute of Optics, 2010. [Online]. Available: <https://search.proquest.com/docview/762414263?accountid=14026>

- [16] J. W. Goodman, *Introduction to Fourier optics*. Roberts and Company Publishers, 2005.
- [17] J. Stoer and R. Bulirsch, *Introduction to Numerical Analysis*. Springer New York, 2002. [Online]. Available: <https://doi.org/10.1007/978-0-387-21738-3>